Reproducibility of Coronary Artery Diameter Assessments in Magnetic Resonance Coronary Angiography: Phantom Study

Paramate Horkaew[1], Jennifer Keegan[2], David N Firmin[2], Guang-Zhong Yang[1*]

[1]Royal Society/Wolfson Medical Image Computing Laboratory, Imperial College, London, UK. [2]Royal Brompton and Harefield NHS Trust, London, UK

{phorkaew, gzy}@doc.ic.ac.uk

Abstract. This report describes the development of a deformable model for the automatic delineation of coronary artery cross-sectional areas with magnetic resonance imaging. The method is validated with coronary artery phantoms of varying diameters and images with different levels of signal-to-noise ratios. The reproducibility of the technique was examined with simulated geometrical shifts and motions during data acquisition. The experimental results indicate a very high reproducibility and low inter-observers variability of the technique, suggesting its suitability for non-invasive assessment of serial changes of vessel dilatation following pharmacological intervention.

1 INTRODUCTION

Change in vessel diameter induced by pharmacological intervention is a potential indicator for endothelial vasodilate dysfunction [1], which is an early marker of atherosclerosis. The prognostic significance of endothelial dysfunction has recently been shown in patients both with [2, 3] and without [3] coronary artery disease. A number of trials have indicated functional improvements in response to lipid-lowering therapies and lifestyle modification [1].

Invasive techniques, such as quantitative coronary angiography (QCA) or intravascular ultrasound (IVUS), are typically used in assessing vessel diameter during catheterization. These techniques commonly suffer from risks associated with clinical complications which have a small but significant mortality rate. As an alternative, Magnetic Resonance Coronary Angiography (MRCA) is emerging as an attractive technique for serial examination of coronary artery dimensions. Although compared to QCA the spatial resolution of MRCA may be limited, and imaging is complicated by both respiratory and cardiac motion, the lack of X-ray is highly beneficial as repeat investigations would not be limited by ionizing radiation regulations. Thus far, there are no reports on inter- and intra- study variabilities of the technique and the reproducibility is unknown.

Preliminary investigation indicated that manual determination of vessel cross-sectional areas introduces considerable variability and the use of MRCA for assessing diameter changes would be greatly advanced by the implementation of a suitable automatic segmentation technique. The pursuit in this direction is currently hampered by the poor spatial resolution achievable, partial volume effect and image degradation resulting from residual cardiac and respiratory motion. By using a set of specially created phantoms, the purpose of this study is to determine the reproducibility of MRCA and the accuracy of an automatic technique for quantifying coronary diameter.

2 MATERIAL AND METHODS

2.1 Image Acquisition

All images for this study were acquired on a Siemens Sonata scanner with maximum gradient strength of 40 mT/m and maximum slew rate of 200 mT/m/ms on each axis independently. The phantoms consisted of 3 straight tubes filled with diluted copper sulphate solution. The diameters of the tubes were 3.11mm, 3.67mm and 4.55mm, respectively, representing typical small, medium and large proximal coronary arteries. Cross-sectional segmented FLASH images of the tubes were acquired with an in-plane resolution of 0.49mm x 0.49mm and a slice thickness of 5mm. By varying the acquisition duration, phantom images were acquired at three different levels of signal-to-noise ratio (SNR) – 'low' = 3.4, 'medium' = 6.7 and 'high' = 10.0 – which were representative of the range of SNR levels observed in *in vivo* images of the same resolution. The acquired images were categorised into two simulation groups: (i) to investigate partial volume effects and (ii) to investigate the effects of motion during the data acquisition period. In the first group, for each level of SNR, the tubes were imaged as the field of view (FOV) was shifted by 0.2 mm increments. In particular, the increments for high and low SNR images were 0.0, 0.2, 0.4, 0.6, 0.8, and 1.0 mm in the x direction and 0.0, 0.2, 0.4, 0.6, 0.8 and 1.0 mm in the y direction, which resulted in a total of 11 images. For medium SNR images, the increments were permuted for each of the x and y shifts, thus resulting in a total of 36 images. The second group contains images corresponding to the first group but with different levels of random motion of the imaging FOV applied in the frequency encoding direction during the acquisition period, In this group, a total of 6 acquisitions were performed at each level of SNR with the degree of motion increasing from 0mm to +/-2.5mm in increments of 0.5mm.

2.2 Building Statistical Shape Models

For the automatic quantification of vessel size, a statistical deformable shape model was used for this study. Unlike the traditional low-level image processing techniques, image segmentation based on deformable models [4, 5] is capable of extracting shapes by exploiting *a priori* knowledge about the size and shape of anatomical structures. It can account for significant variability of biological structures over time

and across different individuals. The Active Shape Model (ASM) [5, 6], for instance, represents a parametric deformable structure based on statistical modelling of global shape variations derived from a training set. During segmentation, the model iteratively deforms to fit to unseen objects but with deformation constrained by principal modes of variation as dictated by the training set. A variation of the ASM was implemented for this study for assessing both the inter- and intra- study variabilities of MRCA by using the aforementioned phantom image data sets.

An experienced observer was asked to delineate the cross-section of the vessels on 65 high-resolution *in vivo* segmented FLASH images. Each cross-section was then modelled as a parametric contour, uniformly sampled with 45 control points. To ensure that the principal modes of variation recovered by ASM reflects the intrinsic shape variation of the training data, the initial pose of the training contours needs to registered. The problem can be formulated as giving **m** set of vector samples $\{\mathbf{x}_i\}_{i=1}^{m}$ to determine rotation $\boldsymbol{\theta}_i$, scaling $\mathbf{s}_i$, and translation $(\mathbf{t_x}, \mathbf{t_y})_i$ such that the following LMS error is minimised:

$$E = (\mathbf{x}_r - M(s_i, \theta_i)[\mathbf{x}_i] - t_i)^T (\mathbf{x}_r - M(s_i, \theta_i)[\mathbf{x}_i] - t_i) \tag{1}$$

In Equation (1), parameters M and $\mathbf{t}$ are given by,

$$M(s_i, \theta_i)\begin{bmatrix} x_{ik} \\ y_{ik} \end{bmatrix} = s_i \begin{bmatrix} \cos\theta_i & -\sin\theta_i \\ \sin\theta_i & \cos\theta_i \end{bmatrix} \begin{bmatrix} x_{ik} \\ y_{ik} \end{bmatrix}$$

and

$$\mathbf{t}_i = \begin{bmatrix} t_{x1} & t_{y1} & \cdots & t_{xK} & t_{yK} \end{bmatrix} \tag{2}$$

where $K = 45$ is the dimension of a given sample indexed by k. This leads to a set of four linear equations

$$\begin{bmatrix} X_i & -Y_i & 1 & 0 \\ Y_i & X_i & 0 & 1 \\ Z & 0 & X_i & Y_i \\ 0 & Z & -Y_i & X_i \end{bmatrix} \begin{bmatrix} s\cos\theta_i \\ s\sin\theta_i \\ t_x \\ t_y \end{bmatrix} = \begin{bmatrix} X_r \\ Y_r \\ C_1 \\ C_2 \end{bmatrix} \tag{3}$$

where,

$$X_i = \sum_k x_{ik} \qquad C_1 = \sum_k (x_{ik}x_{rk} + y_{ik}y_{rk})$$

$$Y_i = \sum_k y_{ik} \qquad C_2 = \sum_k (x_{ik}y_{rk} - y_{ik}x_{rk})$$

$$Z = \sum_k (x_{ik}^2 + y_{ik}^2)$$

The pose parameters $\boldsymbol{\theta}_i$, $\mathbf{s}_i$ and $\mathbf{t}_i$, can therefore be solved by using standard matrix manipulation. In this study, an iterative scheme was used.

In order to capture the principal modes of variation of the aligned shapes, Principal Component Analysis (PCA) was applied to the covariance matrix of the training set so that a statistical Point Distribution Model (PDM) [5] can be derived. The PDM forms a linear space where any given sample can then be approximated up to a given accuracy by using a linear combination of orthogonal basis, *i.e.*,

$$\mathbf{x} = \bar{\mathbf{x}} + \mathbf{P}_s \mathbf{b}_s \tag{4}$$

where $\bar{\mathbf{x}}$ is the mean shape, $\mathbf{P}_s$ is a set of orthogonal modes of variation and $\mathbf{b}_s$ is a set of shape parameters. The derived PDM represents a robust parametric deformable structure, which captures the plausible variations of the training set.

2.3 Image Analysis

To improve the quality of the image data, structural adaptive anisotropic filtering [7] was applied to each image prior to segmentation. Unlike a conventional isotropic filter, such as the Gaussian kernel, this filter provides satisfactory results even for low SNR cases while still preserving detailed structural features. After the filtering, each image was zoomed (×6) and histogram equalised, that is,

$$\begin{aligned} I'(\mathbf{x}) &= \begin{cases} \hat{I}(\mathbf{x}), & \hat{I}(\mathbf{x}) \le 1.5 I(\mathbf{x}) \\ 1.5 I(\mathbf{x}), & \text{otherwise} \end{cases} \\ \hat{I}(\mathbf{x}) &= I_{\max} \int_0^{I(\mathbf{x})} p_I(u) du \end{aligned} \tag{5}$$

where $I(\mathbf{x})$ is the image intensity value at location $\mathbf{x}$ and p is the probably density function on the intensity histogram. The constraint factor *1.5* in (5) controls the upper-limit of histogram stretching. Cross-sectional area of each tube was then determined by using the statistical shape model [5]. The user was first required to mark the approximate centre of the vessel, local deformation was then applied by iteratively varying the first 7 modes of variation based on the ASM approach until convergence. The closed form solution to this minimization problem is given by the projection of the residual vectors onto the eigenspace, that is,

$$\begin{aligned} \mathbf{b}^{i+1} &= \mathbf{b}^{i} + \mathbf{P}^T d\mathbf{x}^i \\ \mathbf{x}^{i+1} &= \mathbf{x}^{i} + \mathbf{P}\mathbf{b}^{i+1} \end{aligned} \tag{6}$$

where $\mathbf{b}^i$ is the shape parameter at the i^{th} iteration, $\mathbf{P}$ is a matrix containing the eigenvectors which describe the principal modes of variation and $d\mathbf{x}^i$ is the residual vector. The back projection is to ensure that the new generated realisation is not only fitted with the image data but also satisfied by the variations found in the training. The remaining shape variation of the contour was then captured by using a local search algorithm based on a medialness function [8] defined by the following integral:

$$M(\mathbf{s}) = \oint_{\mathbf{s}} B(\mathbf{s}_t, \mathbf{u}_t, \sigma) dt \tag{7}$$

where, at a given scale σ, *B* is defined as

$$B(\mathbf{p}, \mathbf{u}, \sigma) = \|\nabla L(\mathbf{p}, \sigma)\| \left| \frac{\nabla L(\mathbf{p}, \sigma)}{\|\nabla L(\mathbf{p}, \sigma)\|} \bullet \mathbf{u} \right|^n \tag{8}$$

In (7), *L* (p, σ) is the filtered version of the image intensity distribution after convolution with a Guassian kernel with standard deviation σ. The constant *n* specifies the amount of directional weighting of the boundary operator. The values of $n = 2$ and $\sigma = 1$ were used for this study.

2.4 Assessment of Errors

Bland Altman analysis was performed to assess both intra and inter observer variability. Intra-observer variability (reproducibility) was calculated as the standard deviation of the signed differences of vessel diameter measured on two occasions on low SNR images as the FOV was shifted by 0, 0.2, 0.4, 0.6, 0.8 and 1.0 in *x* and *y* directions. The low SNR dataset was chosen as a 'worst case' dataset. Inter-observer variability was determined for both high and low SNR datasets as the standard deviation of the signed differences of the vessel diameter measured by two independent observers.

To determine the effect of motion on the segmentation result, the standard deviations of tube diameters (as a percentage of the mean) were calculated with different levels of motion applied during image acquisition as described in 2.1.

3 RESULTS AND DISCUSSION

In Fig. 1, (a) represents a set of images with different levels of SNR, (b) illustrates images acquired with high SNR and different amount of translation, and (c) shows the same high SNR acquisition but with different levels of motion during acquisition. Based on the 65 training samples used in the experiment, Fig. 2 illustrates the statistical variation captured by the first three modes of PCA with the two extremes varied by $\pm 3\sigma$. It is evident that elliptical variation due to non-perpendicular cross-section is well captured by the model. The actual program interface used for both *in vitro* and *in vivo* validation is illustrated in Fig. 3. For all results presented here, the zoom factor used was kept as $\times 6$.

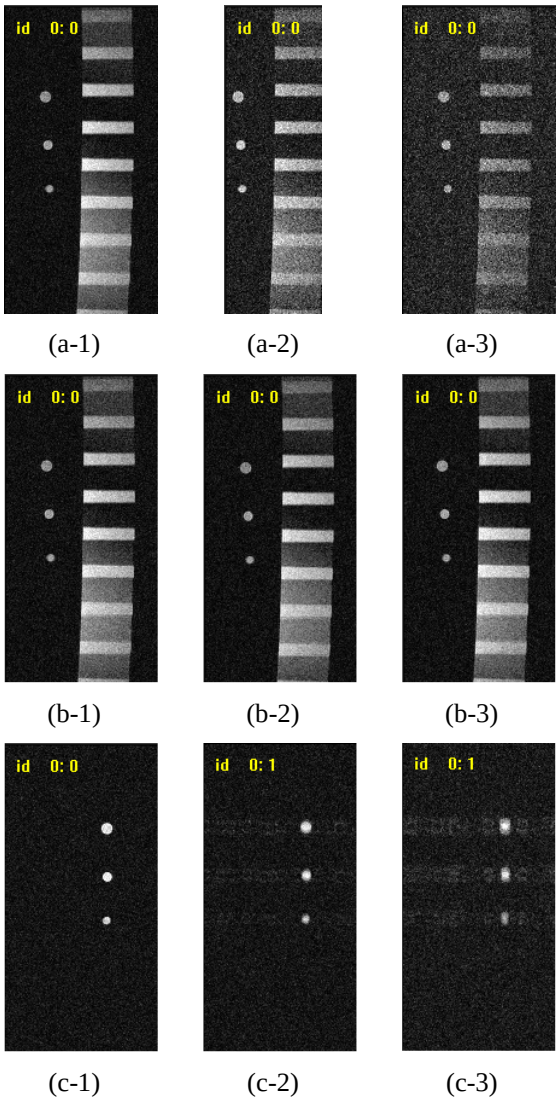

Figure 1. (a-1)-(a-3) Images acquired with low, medium, and high SNRs. (b-1)-(b-3) High SNR images with simulated FOV shift at 0.0, 0.4 and 1.0 mm along the ?? direction. (c-1)-(c3) The same high SNR acquisition but with 0.0, 1.0, and 2.0 mm motions.

For detailed error analysis, a total 76 images were analysed. Fig. 4 plots the variation of the measured tube diameter from the high SNR images with FOV shifted from 0.0 to 1.0 mm in both *x* and *y* directions with 0.2mm increments. The standard deviation/mean for large, medium and small size tubes was 1.1, 1.05 and 1.32%, respectively. Similarly, Figs. 5 and 6, plot the tube diameters for different FOV shifts

for the medium and low SNR images. Unlike in high and low SNR cases, there were 36 images altogether for medium SNR, corresponding to permuted *x* and *y* translations. In this case, the standard deviation/mean for large, medium and small size tubes was 1.32, 1.27 and 2.01%. The corresponding values for low SNR images were 1.65, 1.57 and 2.00%, respectively. It is evident that the standard deviation decreases as SNR and vessel size increase.

The scatter plots in Fig 7 demonstrate the inter-observer variability of the measured vessel diameter by two independent observers on high (left) and low (right) SNR images, respectively. The regression in both cases indicates a good correlation between the two measurements, implying the robustness of the algorithm against noise. Further analysis showed the reproducible of the algorithm with the mean (+/- SD) difference between repeat analyses of the high-resolution images being 0.0 mm, +/-0.0024, +/-0.0059 and +/- 0.0086 mm. These values were measured from low SNR images and quoted for large, medium, and small size vessels respectively. The results of Bland Altman analysis are shown in Fig. 8.

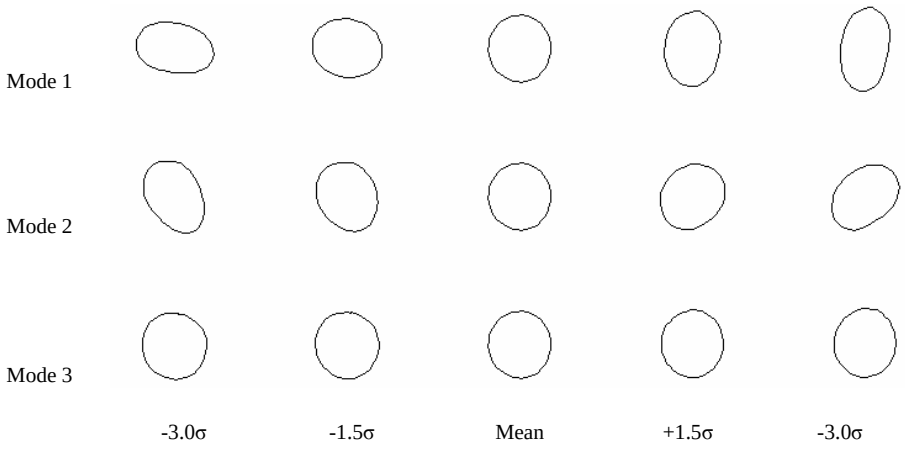

Figure 2. The variation captured by the first three principal modes of variation of the statistical shape model where the shape parameters were varied by ±3σ.

Fig. 9 illustrates the effect of motion on the measured vessel diameters. It can be seen from the graphs that the same degree of applied motion has a similar effect on all tube sizes. The standard deviation is high for the largest tube and decreased as the tube sizes, except in low SNR case where the inverse is true. It is interesting to note that for a given vessel size, the standard deviation with respect to simulated motions does not correlate well with the level of SNR, which seems to imply that the two effects are somewhat decoupled.

In general, good quality data were obtained in all (100%) of the 76 images studied. As such, it should be feasible to use serial magnetic resonance imaging to determine

vessel diameter response to vasodilators, as used in studies of endothelial function or to other pharmacological interventions.

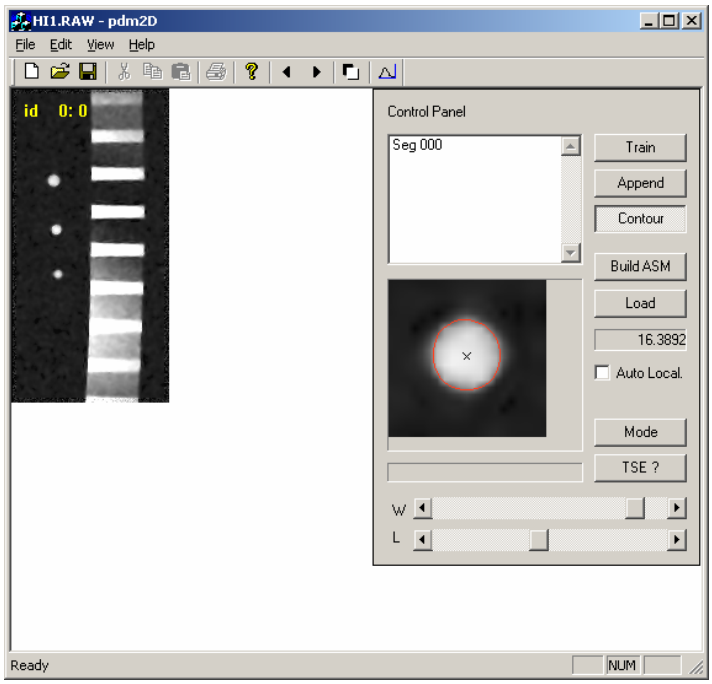

Figure 3. The software interface used for vessel delineation.

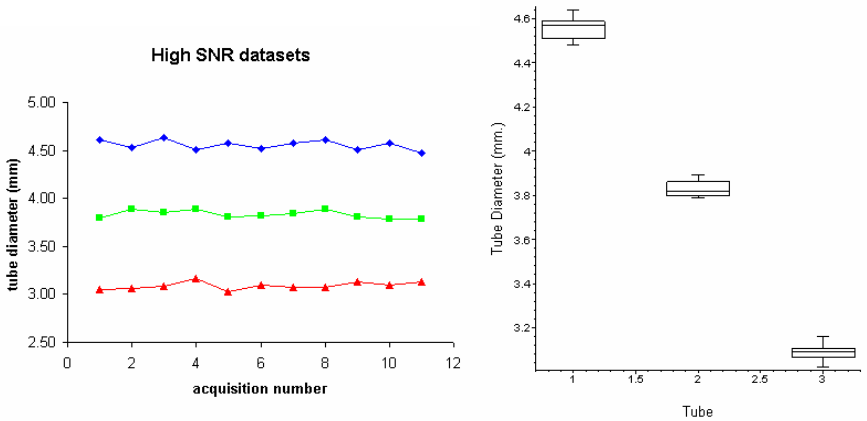

Figure 4. Variations of the measured tube diameters (mm) for high SNR images as the FOV was shifted by 0.0, 0.2, 0.4, 0.8, and 1.0 mm in *x* and *y* directions.

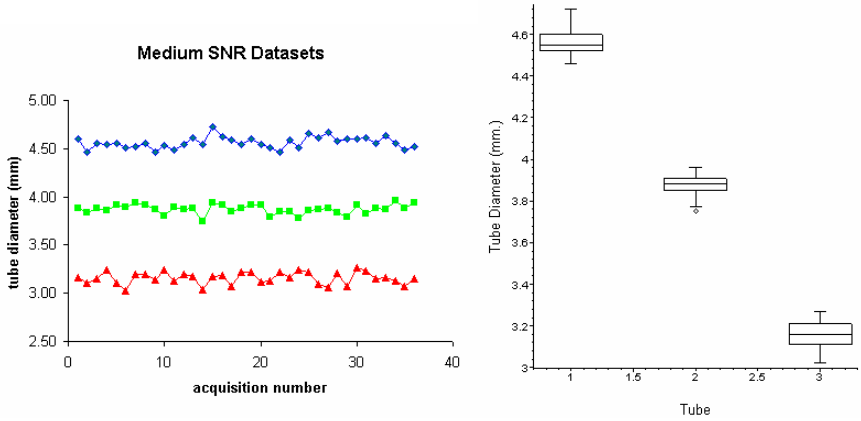

Figure 5. Variations of the measured vessel diameters (mm) for medium SNR images as the FOV was shifted by 0.0, 0.2, 0.4, 0.8, and 1.0 mm along the *x* and *y* directions.

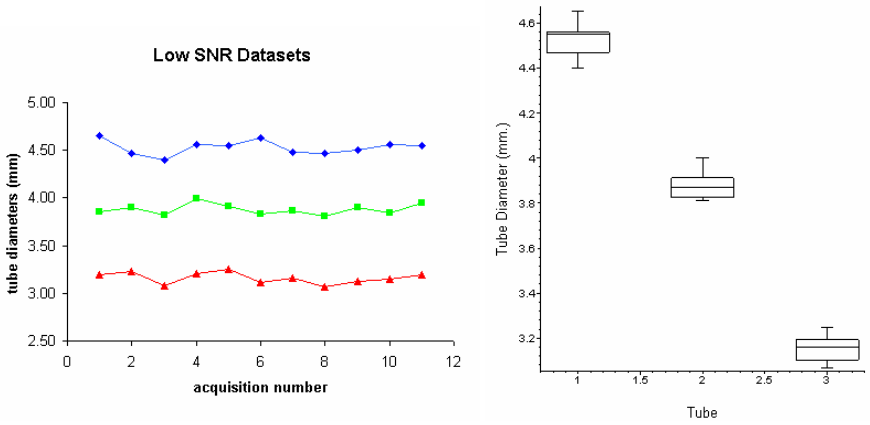

Figure 6. Variations of the measured vessel diameters (mm) for low SNR images as the FOV was shifted by 0.0, 0.2, 0.4, 0.8, and 1.0 mm along the *x* and *y* directions.

4 CONCLUSIONS

Extracting structures from medical images and reconstructing their geometric representations is a challenging task. The presence of noise and motion artefacts has significant influence on the accuracy of structural delineation. In this study, segmented FLASH was chosen as the imaging technique as it is robust and 0.49 mm in-plane resolution was relatively easy to achieve in practical applications. If comparisons are to be made with intravascular ultrasound and quantitative coronary

angiography, it is important to be aware what is being imaged with each technique. Quantitative coronary angiography delineates the vessel lumen whereas intravascular ultrasound images the vessel wall, *i.e.*, the inner boundary of which demarcates the lumen. Dark blood turbo spin-echo delineates the outermost extent of the vessel by imaging the high intensity epi-cardial fat surrounding it whereas segmented FLASH, images both blood (lumen) and vessel wall with the blood signal being increased due to through-plane flow enhancement. To standardise the assessment, we are currently implementing a coupled ASM algorithm that is able to segment both lumen and vessel wall simultaneously.

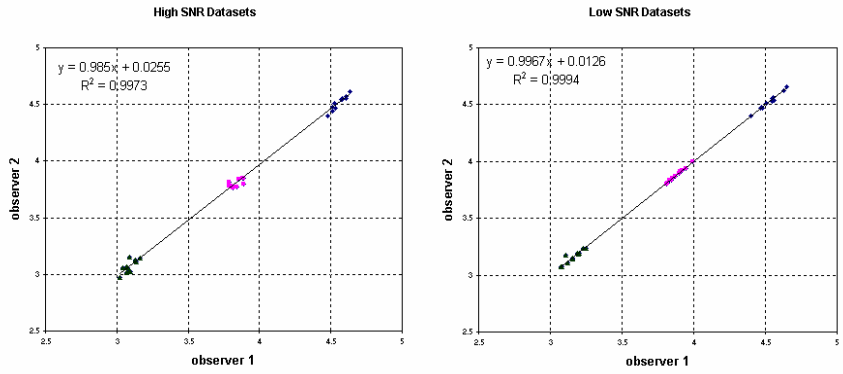

Figure 7. Scatter plots showing the inter-observer variability of the measured vessel diameters on high (left) and low (right) SNR images when FOV is shifted.

Compared to other techniques, MRCA has the major advantages of being non-invasive and without ionising radiation. In this study, it has shown a similar variability to quantitative coronary angiography in serial acquisitions. Of note however, is that as the MRCA images are acquired over a period of approximately 2 minutes, they may be degraded if the heart rate is variable during the scanning period or if the heart rate is substantially increased with pharmacological intervention. This factor, simulated as the motion in this experiment, indicates an ambiguity contributing to the measured results. As a result, further investigation on this issue is required. It is important to note that changes in coronary blood flow may also alter the degree of through-plane enhancement of the blood signal (whilst the vessel wall remains unchanged) and this may alter the appearance of the vessel and the area segmented. For this reason, histogram equalisation was first applied to the image to reduce the variations. It should also be taken into account that the images studied here were phantom, and although the range of vessel diameters was large (3.0 mm – 4.8 mm), the absence of disease may have resulted in better image quality than would have been obtained in a population with coronary artery disease.

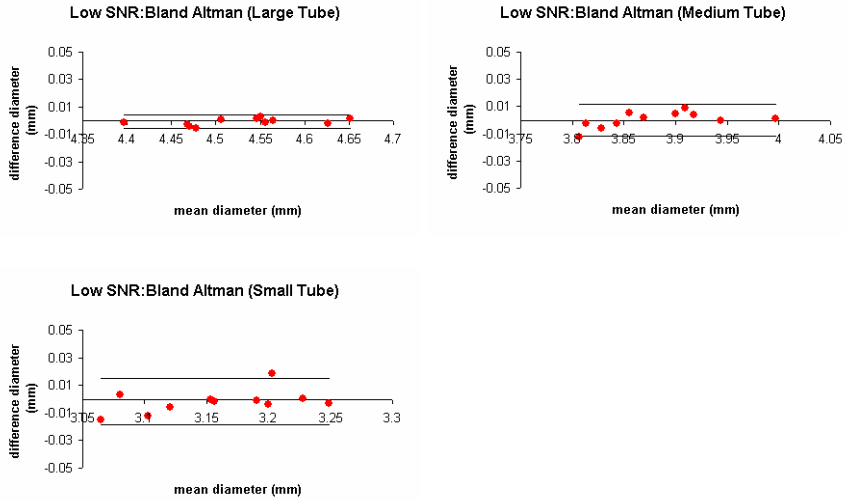

Figure 8. Bland Altman plots showing the reproducibility of the segmentation results as derived from low SNR images when FOV was shifted.

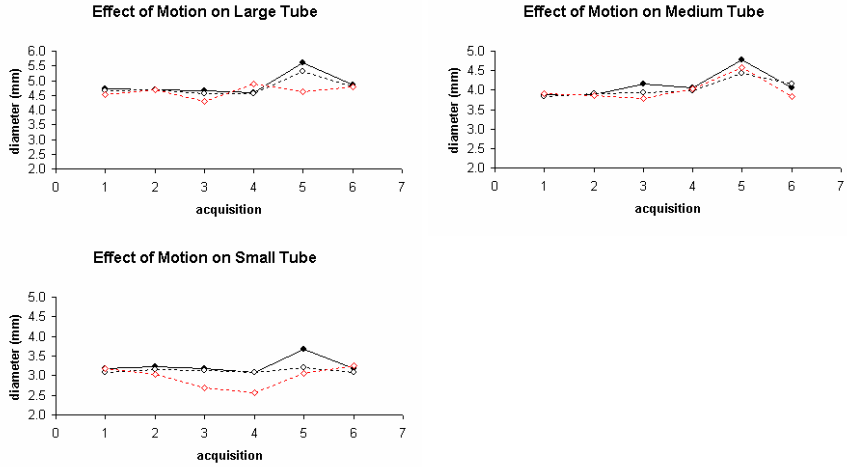

Figure 9. The effect of motion on the measured vessel diameters for images acquired with high (solid line), medium (black-dotted line) and low (red-dotted line) SNRs, where in each graph the acquisition indices correspond to 0, 0.5, 1.0, 1.5, 2.0, and 2.5 mm motion induced during acquisition.

In conclusion, we have developed an automated segmentation technique for the analysis of coronary artery cross-sectional areas, with detailed error analysis applied to coronary artery phantoms. It has been shown that the technique developed has good

inter and intra observer variability under a range of SNR levels, similar to those found in *in vivo* images. It has also been shown that the method is relatively immune to motion during data acquisition, which may occur due to imperfect respiratory gating. The method developed has a high reproducibility which eliminates the need for manual delineation of the vessels and makes it an ideal candidate for serial assessment of coronary artery images.

Reference:

1 Kinlay S, Ganz P. Role of endothelial dysfunction in coronary artery disease and implications for therapy. Am J Cardiol 1997; 80[Suppl-ll]; 11I – 16I.

2 Suwaidi J, Hamasaki S, Higano S, Nishimura R, Holmes D, Lerman A. Long-term follow-up of patients with mild coronary artery disease and endothelial dysfunction. Circulation 2000; 101: 948 – 954.

3 Halcox J, Schenke W, Mincemoyer R, Prasad A, Waclawiw M, Nour K, Quyyumi A. Prognostic value of coronary vascular endothelial dysfunction. Circulation 2002; 106: 640 – 642.

4 T. McInerney ands D. Terzopoulos, "Deformable models in medical image analysis: A survey," Medical Image Analysis 1, 1996: 91-108.

5 Coots TF, Taylor CJ, Cooper DH, Graham J, Active Shape Models - Their Training and Application. Computer Vision and Image Understanding 1995; 61::38-59.

6 Coots TF, Hill A, Taylor CJ, Haslam J, The Use of Active Shape Models for Locating Structures in Medical Images. Image and Vision Computing 1994; 12: 355-366.

7 Yang GZ, Burger P, Firmin DN, Underwood SR. Structural Adaptive Anisotropic Image Filtering. Image and Vision Computing 1996; 14: 135-145.

8 Rueckert D, Burger P, Forbat SM, Mohiaddin RH, Yang GZ. Automatic tracking of the aorta in cardiovascular MR images using deformable models. IEEE Transactions on Medical Imaging 1997; 16: 581-590.